

# Estimating inundation extent using CYGNSS data: A conceptual modeling study



Clara Chew<sup>a,\*</sup>, Eric Small<sup>b</sup>

<sup>a</sup> University Corporation for Atmospheric Research, 3090 Center Green Dr, Boulder, CO 80301, United States of America

<sup>b</sup> Department of Geological Sciences, University of Colorado, 2200 Colorado Ave, Boulder, CO 80309, United States of America

## ARTICLE INFO

**Keywords:**  
Hydrology  
Flooding  
GNSS-R  
Inundation  
CYGNSS

## ABSTRACT

Mapping inundation dynamics and flooding extent is important for a wide variety of applications, from providing disaster relief and predicting infectious disease transmission to quantifying the effects of climate change on Earth's hydrologic cycle. Due to the rapid and highly spatially heterogeneous nature of flooding events, acquiring data with both high spatial and temporal resolutions is paramount, yet doing so has remained a challenge in satellite remote sensing. The potential for Global Navigation Satellite System-Reflectometry (GNSS-R) to help address this challenge has been explored in several studies, the bulk of which use data from the Cyclone GNSS (CYGNSS) constellation of GNSS-R satellites. This work presents a simple forward model that describes how surface reflectivity measured by CYGNSS should change due to flooding for different land surface types. We corroborate our model findings with observations from the Amazon Basin and Lake Eyre, Australia. Both the model and observations indicate that the relationship between surface reflectivity and surface water extent strongly depends on the micro-scale surface roughness of the land and water. We show that the increase in surface reflectivity due to flooding or inundation is greatest in areas where the surrounding land has dense vegetation. In areas where the land surface surrounding inundated areas is perfectly smooth, the increase in surface reflectivity due to flooding is not as strong, and confounding effects of soil moisture and water roughness could lead to large uncertainties in resulting surface water retrievals. However, even a few centimeters of surface roughness will result in several dB sensitivity to surface water, provided that the water is smoother than the land surface itself.

## 1. Introduction

Mapping the presence of surface water and quantifying how its extent changes with time is important for scientific and societal applications. High-resolution, rapidly-updated data describing the evolution of floodwaters during severe weather events are needed for first responders and governmental agencies (Gillespie et al., 2007; Schumann et al., 2007). The combined effect of the predicted acceleration of the hydrologic cycle due to climate change, sea level rise, and the increase of population in coastal and other flood-prone areas will likely increase the demand for such data in the future (Durack et al., 2012; Huntington, 2006). In the tropics, mapping seasonal inundation can lead to better predictions of malarial and other infectious disease transmission (Baqir et al., 2012). And, quantifying the collapse of wetlands around the world is critical, as many of the wetlands that provide economic and ecological benefits to surrounding communities are rapidly disappearing (Gopal, 2013).

There are several ways to map inundation extent, and each method comes with its own advantages and disadvantages. Surface flooding can happen within a matter of hours and can be extremely spatially heterogeneous, so collecting data with both high spatial and temporal resolution is paramount during severe weather events. Long time series are also desired to document lower frequency changes in inundation, like mapping the collapse of wetlands, so data continuity is also important.

Mapping inundation extent is usually accomplished using satellite remote sensing, as in situ observations are sparse and sometimes logistically infeasible due to many wetlands or other inundated areas being in remote regions, or conditions being too dangerous during severe weather events. Satellite remote sensing of surface water can be accomplished using optical, thermal, or microwave instruments. Optical instruments, like Landsat, have been used to create long time series of inundation extent (e.g. Pekel et al., 2016) and are available at high resolution (~30 m). However, the presence of cloud cover in

\* Corresponding author.

E-mail address: [clarac@ucar.edu](mailto:clarac@ucar.edu) (C. Chew).

humid areas or during storms often prevents their use for observing single flooding events. Optical techniques can also not sense water underneath vegetation, which leads to an underestimation of the total amount of surface water. Microwave instruments, which can penetrate cloud cover and some amount of vegetation, are traditionally divided into two categories, either active (monostatic) radars or radiometers. Radiometers can provide data every 2–3 days but with an extremely coarse spatial resolution ( $> 25$  km), and the products generated from these instruments are generally provided in terms of the fraction of a pixel that is inundated (e.g. (Schroeder et al., 2015)). Monostatic radars can provide data with a high spatial resolution ( $\sim 25$  m) but at the expense of temporal resolution ( $> 10$  days) (Geudtner and Torres, 2012). Inundation datasets derived from monostatic radar are usually provided as a binary presence/absence of water for each pixel.

In recent years, increasing attention has been paid to the potential of another type of microwave remote sensing technique to map inundation, Global Navigation Satellite System-Reflectometry (GNSS-R). GNSS-R, in effect, repurposes transmitted L-band signals intended for positioning and uses them to remotely sense the Earth's surface. This bistatic radar technique is like monostatic radar in that it measures how a transmitted signal interacts with the Earth's surface. It is different in that it uses a “free” signal source, which significantly decreases the cost of this technique, and the scattering geometry is also different. Monostatic radars send out a signal and measure how the signal bounces back to the receiver. GNSS-R, on the other hand, measures the signal that is scattered in the forward direction towards the receiver (Fig. 1). Because GNSS-R instruments are relatively inexpensive, since they do not require a transmitter, constellations of these instruments can be launched, which significantly reduces the temporal repeat cycle and opens up the possibility for multiple overpasses each day.

One constellation of GNSS-R instruments is already on orbit and has been collecting data since early 2017: the Cyclone GNSS (CYGNSS) mission. CYGNSS was designed to sense ocean surface wind speed to increase understanding of hurricane intensification in the tropics (Ruf et al., 2018, 2012). However, soon after its launch, it was discovered that the data that are collected over land appear to be sensitive to existence of surface water, as Fig. 2 exemplifies. The eight CYGNSS satellites are able to record surface reflections coming from as far north and south as  $\pm 38$  degrees latitude. Due to the continual movement of the eight CYGNSS satellites and the thirty-two Global Positioning System (GPS) satellites that act as the transmitters, the point of reflection on the Earth's surface is constantly changing, which means that the surface is sampled pseudo-randomly. The CYGNSS satellites are each able to record up to four independent reflections at one time, even though reflections from more GPS satellites might be in view. Over the ocean surface the CYGNSS mission has estimated the mean repeat time

to be  $\sim 4$  h (Ruf et al., 2012). The temporal repeat frequency over the land surface is longer, due to the fact that the probable spatial resolution over the land surface is smaller, which results in more time needed between the collection of collocated observations. The spatial resolution is described in more detail below. Generally, after a few days to a week spatial coverage over land is dense enough that only small gaps remain in aggregate maps. Although the CYGNSS satellites themselves may not provide the daily, complete spatial sampling that is desired for flooding applications, they do provide insight into what might be possible with additional GNSS-R satellites or GNSS-R receivers able to record more than four reflections at once, which are already in development.

The purpose of this work is to describe the relationship between a CYGNSS observation and the surface water extent within the CYGNSS footprint. Previous works (e.g., (Chew et al., 2018a, 2018b; Jensen et al., 2018; Morris et al., 2019; Nghiem et al., 2017; Rodriguez-Alvarez et al., 2019)) have matched CYGNSS and other GNSS-R data in specific regions to ancillary remote sensing datasets or in situ observations to show that the GNSS-R data are responding to changes in inundation extent. Here, we will use a simple forward model of reflectivity to characterize the relationship between CYGNSS observations and surface water extent. We will compare results from the model to CYGNSS observations from two benchmark test regions and comment on the potential of using this model as the foundation for a retrieval algorithm to map inundation using CYGNSS data.

## 2. CYGNSS data

The data that CYGNSS records come in the form of delay-Doppler maps (DDMs), and the peak value of each DDM should, in theory, be sensitive to the dielectric constant and the roughness of the surface (Egido, 2013; Masters, 2004). Multiple other studies that use GNSS-R data over land show examples of DDMs (e.g. (Camps et al., 2016; Chew et al., 2016; Clarizia et al., 2009; Foti et al., 2015)), and we invite readers to view these papers for examples. The peak value of the DDM is also going to be affected by other variables unrelated to the reflecting surface, such as the range and antenna gain (De Roo and Ulaby, 1994). We correct for these variables assuming a coherent reflecting surface:

$$P_r = \frac{P^t G^t}{4\pi(R_{ts} + R_{sr})^2} \frac{G^r \lambda^2}{4\pi} \Gamma_{\text{surface}} \quad (1)$$

where:  $P_r$  is the total scattered coherent power (the peak value of the DDM),  $P^t$  is the transmitted RHCP power,  $G^t$  is the gain of the transmitting antenna,  $R_{ts}$  is the distance between the transmitter and the specular reflection point,  $R_{sr}$  is the distance between the specular reflection point and the receiver,  $G^r$  is the gain of the receiving antenna,  $\lambda$

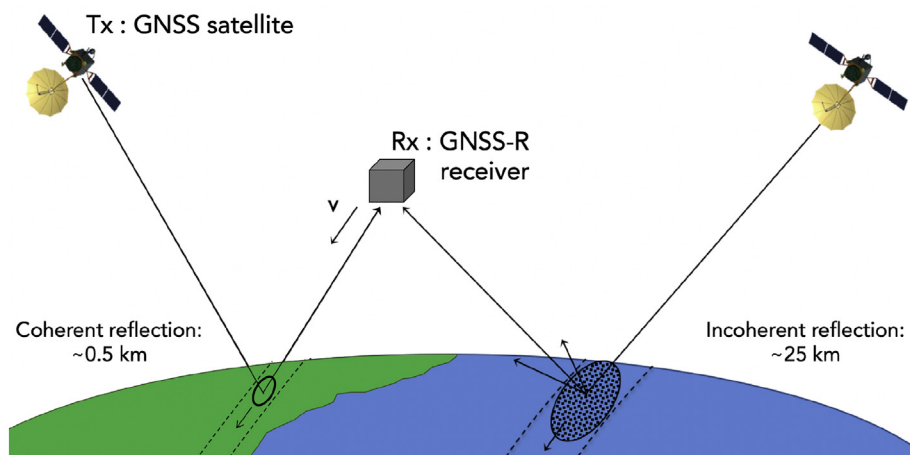


**Fig. 1.** Schematic of the GNSS-R technique. A GNSS satellite (Tx) transmits a signal towards the Earth's surface. Part of this signal reflects in the forward (specular) direction and back into space. A GNSS-R receiver (Rx) onboard a low Earth orbiting satellite, with a downward looking antenna, records this signal. The point on the Earth's surface where the signal reflects depends upon the positions of the transmitting and receiving satellites. The roughness of the surface at the reflection point determines the spatial resolution of the signal, with rougher (smoother) surfaces producing incoherent (coherent) reflections and larger (smaller) spatial footprints. The ocean (blue) is often rougher than land (green), resulting in a larger footprint. The receiver integrates the reflected signal over a period of time, which elongates the spatial footprint in the along-track direction. (For interpretation of the references to colour in this figure legend, the reader is referred to the web version of this article.)

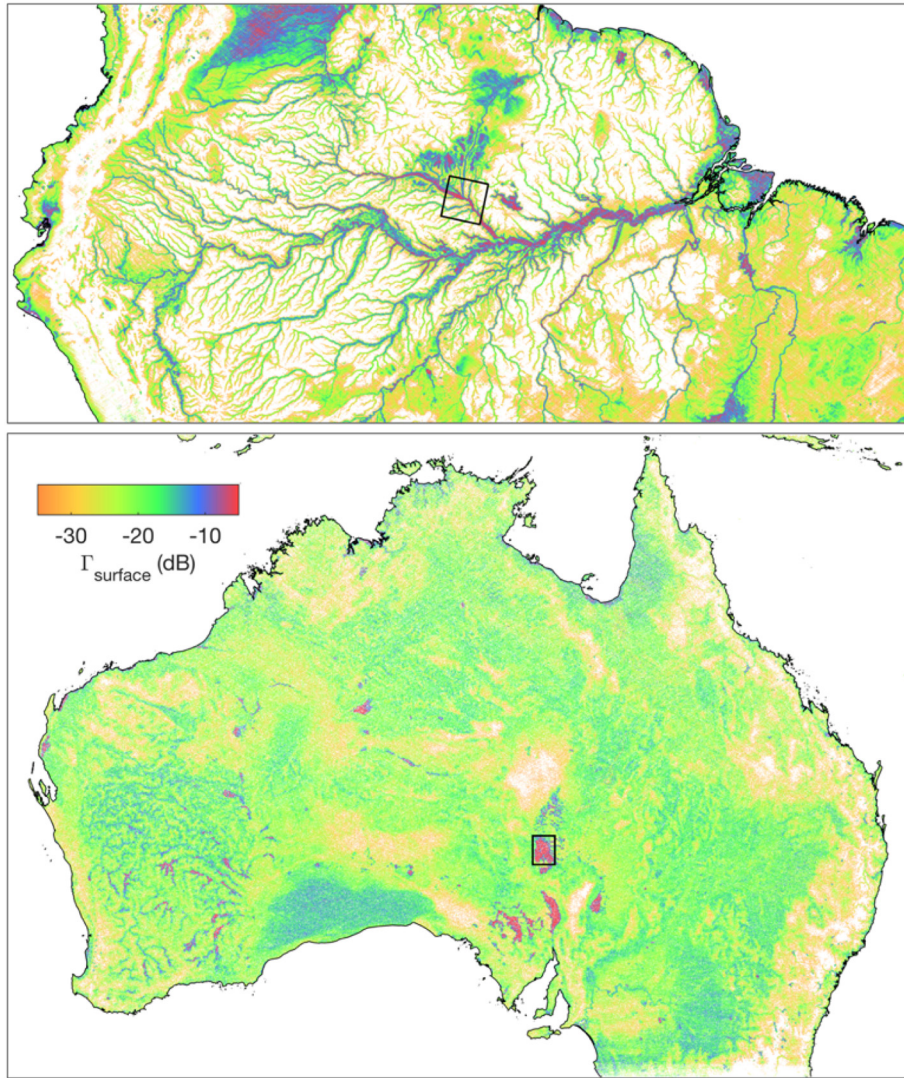


Fig. 2. CYGNSS observations of  $\Gamma_{surface}$  (defined below) over the Amazon basin (top) and Australia (bottom), for 2018. Here, we sorted the observations such that the highest values of  $\Gamma_{surface}$  are plotted on top of observations close by with lower values of  $\Gamma_{surface}$ . Higher values of  $\Gamma_{surface}$  are found over water bodies and saturated land, or over regions without significant topography. Black outlined boxes delineate the two test regions used in this study.

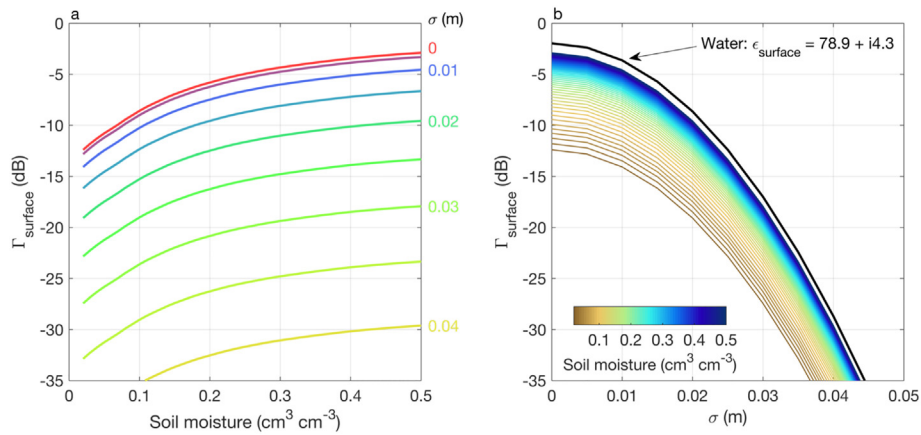


Fig. 3. a. The relationship between soil moisture and  $\Gamma_{surface}$ , for different values of surface roughness. b. The relationship between surface roughness and  $\Gamma_{surface}$  for different values of soil moisture. Also shown is the relationship between surface roughness and  $\Gamma_{surface}$  when the surface has a dielectric constant typical of water.

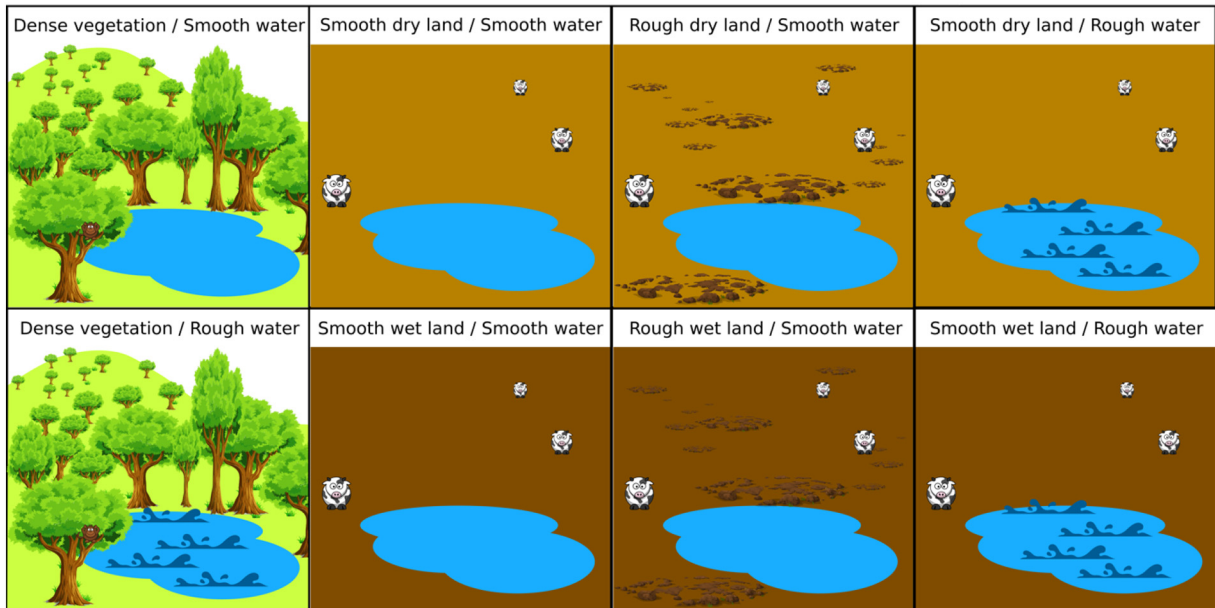


Fig. 4. Depiction of the modeling scenarios used in this study. Parameters used in the model for each scenario are shown in Table 1.

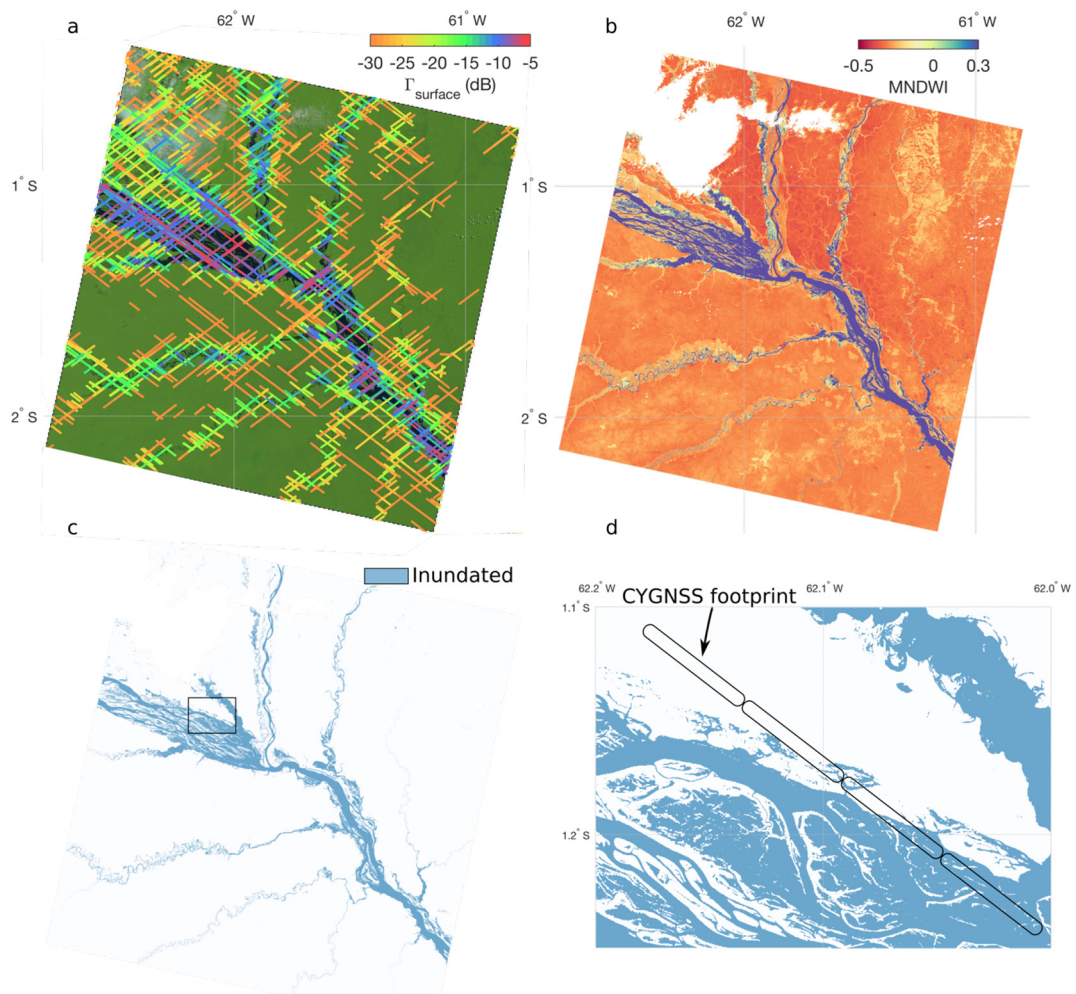
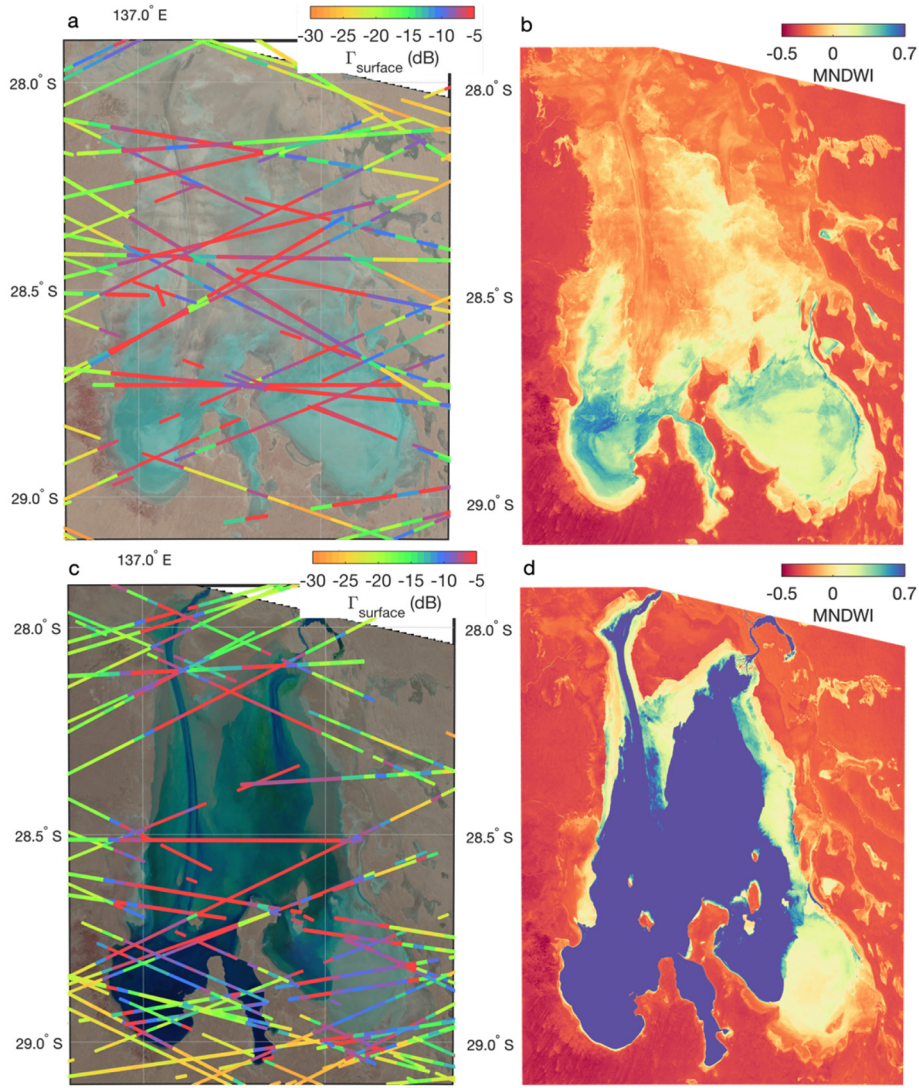


Fig. 5. a. Landsat image of a tributary to the Amazon River (path 232, row 061) on August 6, 2017. CYGNSS observations of surface reflectivity are overlaid for the time period August 6 – September 7, 2017. b. MNDWI derived from the Landsat image using the cloud mask. Colour bar was artificially truncated at 0.3. c. Water mask resulting from thresholding the MNDWI image in (b). The black outlined box is the region shown in (d). d. Close up of the water mask, with examples of CYGNSS footprints overlaid. Footprints may contain a mixture of dry land and open water.



**Fig. 6.** Same as Fig. 5, except for Lake Eyre in Australia, where (a) is a Landsat image (path 099 row 080) acquired on January 13, 2019. Overlaid CYGNSS data are for the time period January 12–14, 2019. (b) MNDWI for (a). (c) Same as (a), except the Landsat data acquired on July 8, 2019. Overlaid CYGNSS data are for the time period July 7–9, 2019. (d) MNDWI for (c). These are only two of the thirty-three Landsat 8 scenes used in this analysis. The water mask derived from (d) is shown in Fig. A2.

is the GPS L1 wavelength (19 cm), and  $\Gamma_{\text{surface}}$  is the reflectivity of the surface. Here, we convert all terms to dB and solve for  $\Gamma_{\text{surface}}$ :

$$\begin{aligned} \Gamma_{\text{surface}} &= 10 \log P_r - 10 \log P^t - 10 \log G^t - 10 \log G^r + 20 \log (R_{\text{ts}} + R_{\text{sr}}) - 20 \\ &\quad \log \lambda + 20 \log 4\pi \end{aligned} \quad (2)$$

Currently, the GPS equivalent isotropically radiated power (EIRP) ( $P^t G^t$ ) is only being minimally corrected for, by using lookup tables of how EIRP should vary according to the specific GPS satellite. However, it is well known that the GPS transmit power can and does vary depending on location and over time. In this paper, we expect variability in  $P^t$  will introduce between 0.24 and 2.5 dB of uncertainty (Gleason et al., 2019; Steigenberger et al., 2019). Future versions of the CYGNSS data are expected to take these variations into account.

Surface reflectivity can also be affected by incidence angle, much in the same way backscatter observations are affected by incidence angle (Clapp, 1946; Mladenova et al., 2013; Ulaby et al., 1978). One can correct for the effect of local incidence angle on  $\Gamma_{\text{surface}}$  with the following:

$$\Gamma_{\text{surface}} = \Gamma_{\text{surface}} - 10 \log \cos^n \theta \quad (3)$$

where  $\theta$  is the angle of incidence, and  $n$  is a parameter, which normally varies between 0 and 2 (Clapp, 1946; Mladenova et al., 2013), with larger values being used for rougher surfaces. Here, we use  $n = 1$  in our corrections of incidence angle, as higher values appeared to overcorrect for incidence angle variations. The average correction using Eq. 3 in the examples we will show was only 1.28 dB and thus does not significantly affect our results.

Because GNSS-R is a relatively new technique, the spatial resolution of the signal over the land surface is still being quantified. Unlike other microwave remote sensing instruments, the spatial resolution of CYGNSS is not determined by the size of the antenna. Instead, it is a function of the roughness of the surface, with extremely rough surfaces producing reflections coming from a larger area than perfectly smooth areas. The published spatial resolution of CYGNSS is  $25 \times 25$  km (Clarizia and Ruf, 2016). This is derived from the assumption that the rough ocean surface produces incoherent reflections as well as the fact that the CYGNSS data processing uses information from several pixels in the DDM surrounding the specular reflection point, which enlarges the total reflected area. However, if the surface is completely smooth and reflections are predominantly coherent, then the spatial resolution is  $\sim 0.5 \times 0.5$  km for a low earth orbiting satellite like CYGNSS, though

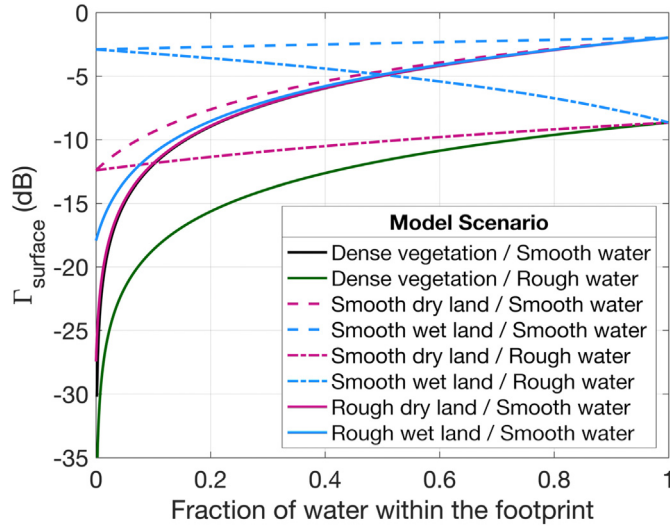


Fig. 7. Model simulations of  $\Gamma_{surface}$  using the scenarios presented in Table 1 and Fig. 2, for an incidence angle of 20 degrees. Model simulations for different incidence angles are shown in Fig. A3.

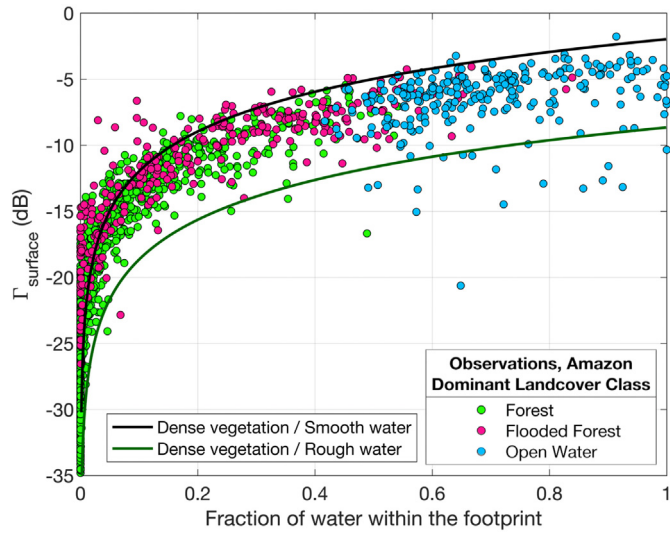


Fig. 8. Observations of  $\Gamma_{surface}$  from CYGNSS in the Amazon basin versus the fraction of water within the CYGNSS footprint, derived from Landsat 8 MNDWI (colored circles).  $\Gamma_{surface}$  observations are colored by their dominant landcover class, obtained from GlobCover 2009 (Defourny et al., 2009). Also shown are the Dense vegetation model simulations (black and green lines). (For interpretation of the references to colour in this figure legend, the reader is referred to the web version of this article.)

this also depends slightly on incidence angle (Katzberg and Garrison, 1996). The CYGNSS satellites themselves introduce an additional complexity in that they integrate the received signal for a period of time, which elongates the spatial footprint along the track. Until mid-2019 a 1-s integration was used, which meant the smallest theoretical footprint was  $7 \times 0.5$  km. After mid-2019, integration time was decreased by half, which decreased the smallest theoretical footprint to  $3.5 \times 0.5$  km. Higher incidence angles will elongate the spatial footprint by a few hundred meters. Here, we assume that the spatial footprint is the smallest theoretical footprint, while accounting for incidence angle. This means that we neglect significant surface roughness (root mean square (RMS) surface height deviation  $> 5$ – $7$  cm), which would lead to predominantly incoherent scattering (Balakhder et al., 2019).

### 3. Model description

#### 3.1. Model foundation

Models that describe the backscattering of microwave signals from monostatic radars or the emission of microwaves for passive radiometry have been studied for several decades. The majority of backscatter models are concerned primarily with how signals scatter off of vegetation canopies, and nearly all of these describe a canopy in terms of individual geometric components of the canopy: leaves, branches, tree trunks, etc. The most complex microwave model could have several parameters describing things like leaf shape and trunk diameter (e.g., (Burgin et al., 2011; Lang and Sighu, 1983; Ulaby et al., 1990)). Most models that describe the forward-scattering GNSS-R scenario over land are nascent in comparison and have not undergone extensive validation. The majority of the existing models have been converted from discrete backscattering models (e.g., (Ferrazzoli et al., 2011; Pierdicca et al., 2014)) or were developed for ocean surface applications (O'Brien and Johnson, 2017).

Our model, by comparison, is more conceptual and simple to run, requiring few parameters. The goal of using this model is not to explore the details of GNSS-R signal scattering. Rather, the purpose is to consider possible explanations for if and why the relationship between reflectivity and inundation exhibits spatial variations. Our model requires the following parameters: the fraction of a pixel that is inundated, the soil moisture and texture of the land surface that is not inundated, the dielectric constant of water, and the micro-scale roughness of both the land surface and the water. The output of the model is the reflectivity of the surface ( $\Gamma_{surface}$ ).

$\Gamma_{surface}$  is determined by the surface dielectric constant and roughness. For a bare surface and assuming that surface is a homogeneous half space, calculating the surface reflectivity is relatively straightforward and is given by the following (Fuks, 2001):

$$r_h = \frac{\sqrt{\epsilon_{air} - \sin^2 \theta} - \sqrt{\epsilon_{surface} - \sin^2 \theta}}{\sqrt{\epsilon_{air} - \sin^2 \theta} + \sqrt{\epsilon_{surface} - \sin^2 \theta}} \quad (5)$$

$$r_v = \frac{\epsilon_{surface} \sqrt{\epsilon_{air} - \sin^2 \theta} - \epsilon_{air} \sqrt{\epsilon_{surface} - \sin^2 \theta}}{\epsilon_{surface} \sqrt{\epsilon_{air} - \sin^2 \theta} + \epsilon_{air} \sqrt{\epsilon_{surface} - \sin^2 \theta}} \quad (6)$$

where:  $\theta$  is the incidence angle of the incoming GNSS signal,  $\epsilon_{air}$  is the dielectric constant of air (1.0), and  $\epsilon_{surface}$  is the dielectric constant of the surface at L-band. For water,  $\epsilon_{surface}$  is high ( $78.9 + 4.3i$  (Kaatze, 1989)). For soil,  $\epsilon_{surface}$  will vary depending on the soil moisture of the surface and the soil characteristics, and these relationships are relatively well known and can be determined from either lookup tables or theoretical equations (e.g. (Dobson et al., 1985; Hallikainen et al., 1985)).  $r_h$  and  $r_v$  are the horizontal and vertical reflection coefficients, respectively.  $r_h$  and  $r_v$  can be converted to left-hand circular polarization (LHCP, which is the polarization of the GNSS-R antenna) via the following equation:

$$r_{lhcp} = 0.5(r_v - r_h) \quad (7)$$

We then calculate the reflectivity, and convert it to dB:

$$\Gamma_{surface} = 10 \log_{10} |r_{lhcp}|^2 \quad (8)$$

Optionally, micro-scale surface roughness can be included in the calculation of the reflection coefficient:

$$r_{lhcp,rough} = S_r \times r_{lhcp} \quad (9)$$

where  $S_r$  is the surface roughness coefficient based on the modified physical optics model (Bahafza, 2005; De Roo and Ulaby, 1996):

$$S_r = \exp(-2[2\pi\sigma \cos \theta / \lambda]^2) \quad (10)$$

and  $\sigma$  is the RMS of the surface height deviations.

Measurements of  $\sigma$  are lacking due to the significant amount of time

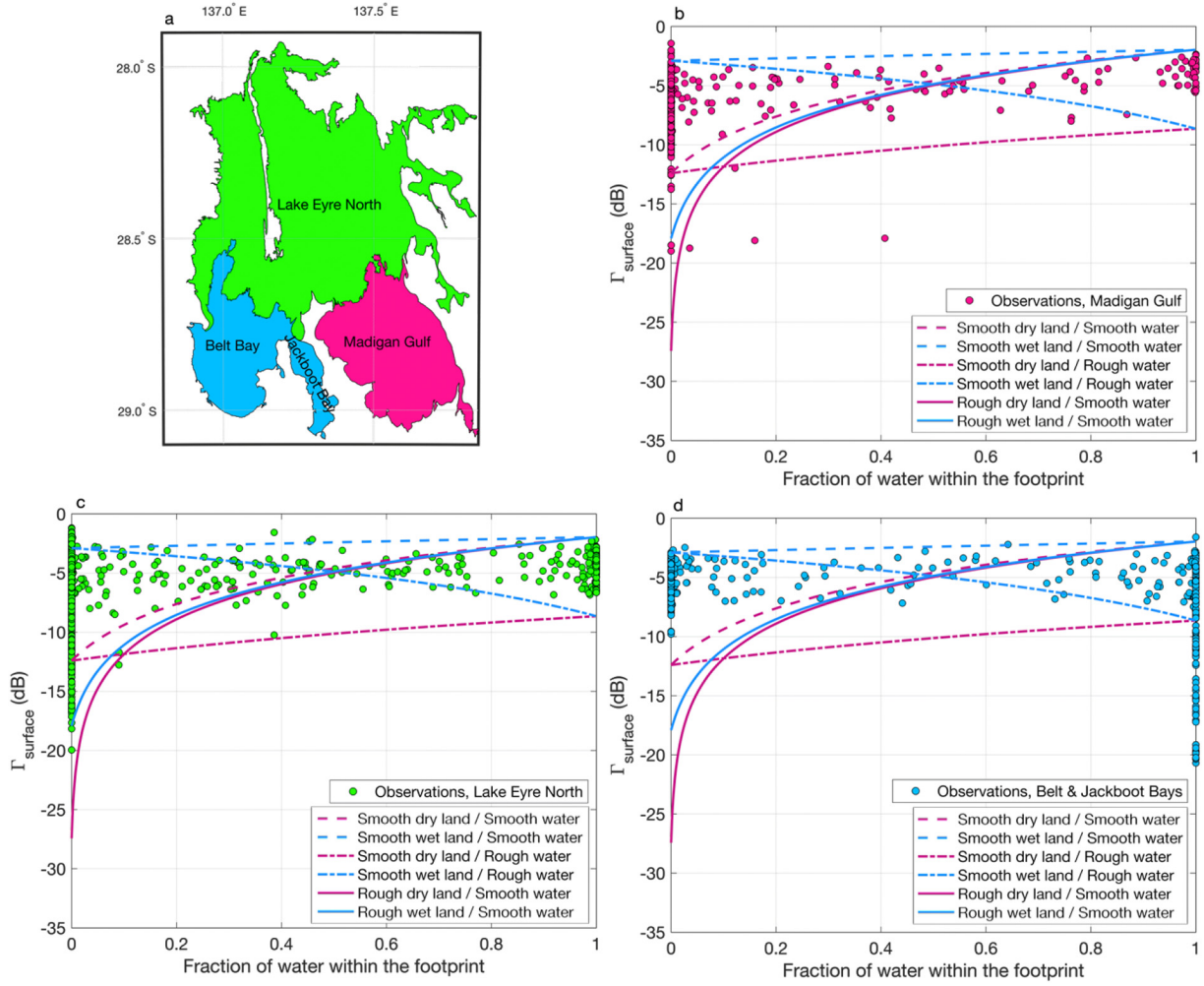


**Fig. 9.** The observed relationship between  $\Gamma_{surface}$  and the fraction of water within an individual CYGNSS footprint for Lake Eyre. (a) The three sub-regions of Lake Eyre. (b) Observations from Madigan Gulf. (c) Observations from Lake Eyre North. (d) Observations from Belt and Jackboot Bays. Also shown are the model simulations from Table 1/Figs. 3 and 4 that best match the trends seen in the observations for a typical incidence angle of 20 degrees.

required to obtain them, and also because different techniques of measuring  $\sigma$  often produce different results (Thomsen et al., 2015). Other microwave remote sensing satellites (e.g. NASA's Soil Moisture Active Passive mission (SMAP)), which also require knowledge of  $\sigma$ , tend to parameterize  $\sigma$  using assumptions based on landcover class (Peng et al., 2019). We will not do that here, as an appropriate parameterization of  $\sigma$  for GNSS-R would itself be a serious undertaking. Published values of  $\sigma$  tend to be less than 2 cm for natural surfaces, with higher values of  $\sigma$  (2–5 cm) for ploughed agricultural fields (Hornbuckle et al., 2017; Snapir et al., 2014; Thomsen et al., 2015).

Examples of model output of  $\Gamma_{surface}$  for different combinations of realistic input values of  $\epsilon_{surface}$  and  $\sigma$  are shown in Fig. 3. Here, we show  $\epsilon_{surface}$  converted to soil moisture for a loamy soil, with values obtained from (Dobson et al., 1985). Fig. 3 shows that  $\Gamma_{surface}$  increases as soil moisture (and hence,  $\epsilon_{surface}$ ) increases, and  $\Gamma_{surface}$  decreases as surface roughness increases. These relationships are non-linear. However, in realistic scenarios where soil moisture has a more limited range, they might be approximated as linear, as was done in (Chew and Small, 2018). Observations of  $\Gamma_{surface}$  from CYGNSS in the vicinity of in situ soil moisture probes show good agreement with the model simulations (see Appendix for examples). Also shown in Fig. 3b is the relationship between  $\Gamma_{surface}$  and surface roughness for the case when  $\epsilon_{surface}$  is set to a typical value for fresh water ( $78.9 + 4.3i$  (Kaatzte, 1989)). The relationship is very similar to that simulated for a saturated soil, although the magnitude of  $\Gamma_{surface}$  is higher for all values of surface roughness.

### 3.2. Modeling heterogeneous footprints

Thus far, we have described how to calculate the reflectivity for a surface of a given dielectric constant and modulate it for a given value of micro-scale surface roughness using equations and formulations that are found in many journal articles and textbooks. However, the relatively large spatial footprint of CYGNSS all but guarantees that there will not just be one dielectric constant within its field of view over land. A more complicated model might consider the surface to be made up of thousands of facets and assign different values of  $\epsilon_{surface}$  for individual facets or groups of facets. Instead, what we will do here is categorize the surface as either inundated or not inundated and calculate the fraction of the surface that falls into either category. Assuming we know the dielectric constant and roughness of both the inundated and not inundated fractions, we will calculate the surface reflectivity for the entire surface as the weighted average of the reflectivities of the inundated and non-inundated areas, weighted by their fractional coverage:

$$\Gamma_{surface} = \rho \times \Gamma_{inundated} + (1 - \rho) \times \Gamma_{dry} \quad (11)$$

where:  $\rho$  is the fraction of the CYGNSS footprint that is inundated,  $\Gamma_{inundated}$  is the reflectivity of the water, and  $\Gamma_{dry}$  is the reflectivity of the footprint that is not inundated. Here, although the subscript is *dry*, it does not mean that it cannot have a high soil moisture content.

### 3.3. Model scenarios

We will investigate whether the linear mixing assumption presented in Eq. 11 is correct, using several simple model scenarios and comparing the results to actual observations. Fig. 4 depicts several different scenarios that will be simulated by our model. These scenarios were chosen because they represent end members for what might be encountered in the real world: some model scenarios will represent extremely vegetated environments, and others will represent perfectly planar scenes, which would rarely occur in nature. In the first scenario we assume that there is some amount of water within the CYGNSS footprint, and that surrounding this water is land that is too vegetated to produce any forward-scattered signal for CYGNSS to sense (Dense vegetation / Smooth water). Real-world analogues of this scenario could be thought of areas in the Amazon or Central Africa. In this scenario, we will see whether our assumption holds that there is not significant forward scattering without water underneath the vegetation. In a complementary scenario, we will see what effect slight wind-roughening of the water has on  $\Gamma_{\text{surface}}$  (Dense vegetation / Rough water).

Other scenarios modeled are also scenes with a prescribed amount of open water, but the land surrounding that water is either flat enough or bare enough that at least some amount of signal can be sensed by CYGNSS. For these scenarios, we will change soil moisture, soil roughness, and the roughness of the water itself to see the effects on  $\Gamma_{\text{surface}}$ . These scenarios are also shown in Fig. 4.

Table 1 shows the parameters used in each model scenario. Constant parameters used across scenarios are the GPS wavelength (0.19 m), the dielectric constant of water ( $78.9 + 4.3i$  (Kaatze, 1989)), and a loamy soil texture. Except for the Dense vegetation scenarios, model simulations were run varying the fraction of open water in the footprint from 0 to 1. For the Dense vegetation scenarios, a fractional water value of 0 produces no reflectivity, so these simulations were run for values between 0.015 and 1. Simulations were all run assuming an incidence angle of 20 degrees (mode of CYGNSS incidence angle observations  $\sim$  = 25 degrees). Results for model simulations run using different incidence angles are contained in the Appendix.

### 4. Corroboration data

In order to corroborate our model, we must compute the extent of surface water within the spatial footprint of CYGNSS to compare with real observations of  $\Gamma_{\text{surface}}$ . However, there is no operational surface water dataset or map that is both concurrent with CYGNSS and exists on a similar spatial scale. Microwave remote sensing inundation datasets usually rely heavily on radiometers, which have a spatial resolution that is too coarse to be effectively compared with CYGNSS (e.g., (Du et al., 2018; Schroeder et al., 2015)). Datasets derived from optical remote sensing instruments like Landsat (e.g. the Global Surface Water Explorer (Pekel et al., 2016)) or MODIS (e.g. the Dartmouth Flood Observatory) are extremely useful to the hydrologic community, though the available data is aggregated over time, either seasonally or

**Table 1**

Parameters used in each model scenario. Soil dielectric constants were obtained from soil moisture content values using (Dobson et al., 1985) assuming a loamy soil. Each scenario was run varying the fraction of open water from 0 to 1.

Model scenario	Soil moisture ( $\text{cm}^3 \text{cm}^{-3}$ )	Soil dielectric constant	Soil / water roughness (m)
Dense vegetation / Smooth water	–	1.0	– / 0
Dense vegetation / Rough water	–	1.0	– / 0
Smooth dry land / Smooth water	0.02	$2.8124 + 0.1087i$	0 / 0
Smooth wet land / Smooth water	0.5	$40.8661 + 4.8221i$	0 / 0
Rough dry land / Smooth water	0.02	$2.8124 + 0.1087i$	0.03 / 0
Rough wet land / Smooth water	0.5	$40.8661 + 4.8221i$	0.03 / 0
Smooth dry land / Rough water	0.02	$2.8124 + 0.1087i$	0 / 0.02
Smooth wet land / Rough water	0.5	$40.8661 + 4.8221i$	0 / 0.02

yearly for the Global Surface Water Explorer, or over 14 days for the Dartmouth Flood Observatory. For our purposes, we need to know the state of surface water for a shorter time period in order to be as concurrent with the CYGNSS data as possible.

In order to accomplish this, here we create our own inundation maps for select regions by deriving the modified normalized difference water index (MNDWI) from Landsat 8 data (Xu, 2006). Modified NDWI (MNDWI) is calculated using the green and middle infrared (MIR) bands recorded by Landsat 8 reflectance values:

$$\text{MNDWI} = \frac{\text{Green} - \text{MIR}}{\text{Green} + \text{MIR}} \quad (4)$$

A threshold is then applied so that any MNDWI values above the threshold are considered to be open water, and anything below the threshold are not. There is no hard and fast rule as to what the threshold should be, and it is generally region specific. We manually determined our thresholds after visually comparing Landsat images of our regions of interest (described below) and resulting water masks. Because the temporal resolution of Landsat 8 is every two weeks, we will only compare concurrent or approximately concurrent CYGNSS data to Landsat 8 scenes.

After we derived the open water masks from the 30 m resolution Landsat 8 data, we used them to calculate the fraction of water within each  $7 \times 0.5$  km CYGNSS footprint. For each CYGNSS observation, we found the Landsat 8 pixels within the CYGNSS footprint and divided the number of open water pixels in the footprint by the total number of pixels in the footprint to derive the fraction of water.

### 5. Benchmark test regions

We chose two different regions to compare Landsat 8 water masks with  $\Gamma_{\text{surface}}$  from CYGNSS. The two regions represent end member scenarios for our modeling effort.

#### 5.1. Amazon basin

The first test region is a portion of the Rio Negro, a tributary of the Amazon (Fig. 5). This Landsat 8 scene has a significant amount of open water surrounded by extremely dense vegetation, so dense that the forward-scattered signal all but completely disappears without water nearby (Fig. 5a). Because the Landsat 8 data cannot sense water underneath vegetation, we will largely ignore the potential confounding effects from obscured water on GNSS-R data and refrain from attempting to quantify attenuation through vegetation canopies for this analysis.

For this benchmark case, we used data from one Landsat 8 tile that is centered at approximately  $-1.3$  deg. S, and  $-61.9$  deg. W. The Amazon Basin is a notoriously cloudy region, and it is relatively rare to find a mostly cloud-free Landsat tile from which to calculate MNDWI. The tile and specific acquisition (August 6, 2017) shown in Fig. 5 is one of the most cloud-free days we were able to find during the time period when CYGNSS data are available. For this specific area, inundation

extent did not change significantly between August 6 and September 7 (the date for the next relatively cloud-free Landsat 8 acquisition), and so we used any CYGNSS data recorded between these two dates and compared them to the water mask derived from the August 6 acquisition. Thus, here we are not looking at changes in inundation over time for a specific location, but instead quantifying how  $\Gamma_{\text{surface}}$  varies spatially due to inundation extent.

The total number of CYGNSS observations was 2123, all of which are shown in Fig. 5a. The corresponding MNDWI data are shown in Fig. 5b. The MNDWI threshold chosen for this tile was 0.3, though altering the threshold had no effect on our conclusions; the resulting water mask is shown in Fig. 5c. Fig. 5d shows a smaller portion of the water mask, with several example CYGNSS footprints overlaid. These footprints illustrate the concept of heterogeneity within each footprint, as the area contained within one footprint can be a mixture of both open water and dry land.

## 5.2. Lake Eyre, Australia

The second test region we chose is Lake Eyre in Australia (Fig. 6). Dry for the majority of the year, Lake Eyre is extremely flat, with large parts of the lake containing salt pans with minimal surface roughness (Fig. 6a). We chose Lake Eyre as our second test region because it is the converse of our first: the salt pan is so flat that one would expect non-inundated land to still produce a detectable reflection. Static 9 km global maps of  $\sigma$  from SMAP, which parameterizes  $\sigma$  based on landcover class, also show that the Lake Eyre region is one of the flattest in the world, with a mean  $\sigma$  of  $\sim 0.6$  cm (Peng et al., 2019). See the Appendix for further discussion of the SMAP static map of  $\sigma$ .

In the summer of 2019, Lake Eyre nearly completely filled, an event that had not been experienced in decades (Fig. 6c). This region is not nearly as cloudy as the Amazon, and so we were able to use several Landsat 8 scenes for this test case. We compared CYGNSS observations that were recorded  $\pm 1$  day of each Landsat acquisition for the full CYGNSS period of record (2017–2019). Thus, in this example we are quantifying how  $\Gamma_{\text{surface}}$  varies through time as Lake Eyre floods and subsequently dries up.

Overall, for Lake Eyre we used 33 Landsat 8 scenes from which to derive water masks from MNDWI and compared them to 3210 CYGNSS reflections. We chose a higher MNDWI threshold for Lake Eyre (threshold = 0.7), as the bare salt flats produce very high MNDWI, even when dry (Fig. 6d). Altering the threshold did not significantly change the conclusions from this analysis (see Appendix for examples).

## 6. Results

### 6.1. Model scenarios

Modeled  $\Gamma_{\text{surface}}$  versus surface water extent is shown in Fig. 7 for the model scenarios described in Fig. 4 and Table 1. The black line shows how  $\Gamma_{\text{surface}}$  varies with increasing surface water extent for the Dense vegetation / Smooth water scenario. As the amount of water increases in the field of view,  $\Gamma_{\text{surface}}$  increases, though not linearly, with the steepest increases occurring when fractional water extent is below  $\sim 0.2$ . Slightly roughening the water results in lower maximum  $\Gamma_{\text{surface}}$  (dark green line, Dense vegetation / Rough water scenario). This indicates that one should expect lower  $\Gamma_{\text{surface}}$  over larger, more wind-roughened bodies of water than over smaller and calmer bodies of water.

Conversely, when there is perfectly flat, smooth land, increasing surface water extent does not produce as significant of an increase in  $\Gamma_{\text{surface}}$  because  $\Gamma_{\text{surface}}$  is already relatively high even when there is no water within the footprint. And, soil moisture has the potential to be a significant confounding variable for scenes with no surface roughness. The difference in  $\Gamma_{\text{surface}}$  between Smooth dry land / Smooth water (dashed pink line) and Smooth wet land / Smooth water (dashed blue

line) is  $\sim 9.5$  dB when the fraction of water within the footprint is zero. This soil moisture sensitivity falls within the bounds of what has been found empirically in previous studies (Chew and Small, 2018). The model shows that it would be difficult to detect an increase in inundation if the soil is smooth and already saturated (Smooth wet land / Smooth water, dashed blue line), since the increase in  $\Gamma_{\text{surface}}$  with surface water extent is very small.

Adding 3 cm of microscale surface roughness (Rough dry and wet land / Smooth water scenarios, pink and blue solid lines, respectively) significantly decreases  $\Gamma_{\text{surface}}$  with respect to the Smooth land scenarios, particularly when fractional water is low. A wet but rough soil (Rough wet land / Smooth water, blue solid line) will produce lower values of  $\Gamma_{\text{surface}}$  than a dry but smooth soil (Smooth dry land / Smooth water, pink dashed line).  $\Gamma_{\text{surface}}$  from a rough and dry soil (Rough dry land / Smooth water, pink solid line) will mimic  $\Gamma_{\text{surface}}$  from the Dense vegetation / Smooth water scenario (black solid line) except when there is no surface water present, and even then, differences are slight. As the amount of water in the scene increases, the influence of soil moisture within the footprint on  $\Gamma_{\text{surface}}$  decreases substantially regardless of the soil surface roughness.

Fig. 7 also shows how  $\Gamma_{\text{surface}}$  should vary for scenes in which the surrounding land is perfectly flat but the water within the scene is roughened (dash-dotted blue and pink lines). When the surrounding land is dry (Smooth dry land / Rough water),  $\Gamma_{\text{surface}}$  will still increase slightly as the footprint fills with roughened water. However, when the surrounding land is saturated (Smooth wet land / Rough water),  $\Gamma_{\text{surface}}$  will actually decrease as the fraction of water in the footprint increases.

### 6.2. Model corroboration

Now we will use observations from our two test regions (the Amazon and Lake Eyre) to corroborate the general trends observed in the model simulations. Unfortunately, there is a dearth of soil moisture and  $\sigma$  observations from which to fully validate the model in our test regions—there are no data consistently quantifying  $\sigma$  of land or water at the 1 cm scale anywhere in the world. It is therefore infeasible to fully validate the model at this time. However, we can corroborate the model by looking to see whether general trends hold in our end member test regions.

Fig. 8 shows how CYGNSS  $\Gamma_{\text{surface}}$  observations change as the fraction of open water within the footprint increases, for our Amazonian test region. Here, observations are colored by their dominant landcover class, as indicated by the GlobCover 2009 dataset. In the Amazon,  $\Gamma_{\text{surface}}$  is very low when there is little to no water in the footprint, but  $\Gamma_{\text{surface}}$  rises quickly when the amount of water in the footprint increases from 0 to 0.2. After  $\sim 0.2$ ,  $\Gamma_{\text{surface}}$  still increases as water is added to the footprint, but much more slowly. This trend falls within the Dense vegetation model scenarios, which are also plotted in Fig. 8. Recall that the Dense vegetation / Smooth water scenario represented a scene where reflectivity was determined only by the presence of completely flat water, and that the Dense vegetation / Rough water scenario represented a scene where reflectivity was determined only by the presence of slightly rough (RMS height = 2 cm) water. It is not unreasonable to assume that the water within the flowing tributary of the Amazon could have some amount of roughness, particularly in the wider stretches of river that are predominantly open water (blue points in Fig. 8). As previously discussed, water masks derived from the optical data used here will not sense water underneath a dense vegetation canopy, and our analysis does not quantify whether or not the CYGNSS data would be able to sense the obscured water, nor does it quantify attenuation through vegetation canopies. However, there is a cluster of observations in Fig. 8 designated as Flooded Forest that have anomalously high values of  $\Gamma_{\text{surface}}$  but with fractional surface water extents below 0.2. It is possible that  $\Gamma_{\text{surface}}$  is higher for these points because the GNSS reflection is responding to water underneath vegetation that the Landsat 8 data was not able to sense.

Fig. 9 shows how observed  $\Gamma_{\text{surface}}$  changes in Lake Eyre due to the presence of surface water. In this figure, we have subdivided Lake Eyre into three different sub-regions, which are indicated by the colored areas in Fig. 9a. We did this because we found that  $\Gamma_{\text{surface}}$  behaved differently as Lake Eyre flooded depending on the sub-region. Both Madigan Gulf and Belt/Jackboot Bays are the major salt pans in Lake Eyre, though Belt/Jackboot Bays are deeper than Madigan Gulf when flooded. Lake Eyre North is not fully covered by salt pans, and thus would be expected to have higher surface roughness in certain areas.

Fig. 9 shows that, across all three sub-regions,  $\Gamma_{\text{surface}}$  is higher than observed in the Amazon when there is little or no water within the footprint. Observations within Madigan Gulf (Fig. 9b) almost fully fall within the model simulations with zero soil surface roughness, which might be expected of a salt flat. There is more variability in  $\Gamma_{\text{surface}}$  in Madigan Gulf when there is no water within the footprint than when Madigan Gulf is completely inundated, which is also in line with the model simulations.

Observations from Lake Eyre North (Fig. 9c), on the other hand, fall within the envelope of simulations where the surface roughness of the land is between 0 and 3 cm. This is expected, since not all of Lake Eyre North is covered by salt pans. All observations of  $\Gamma_{\text{surface}}$  less than  $-12$  dB come from the northeastern and eastern edges of the lake, which appear to contain sand bars and other small topographic features that would introduce roughness. Like Madigan Gulf, as the footprint fills with water, the variability in  $\Gamma_{\text{surface}}$  decreases, and all observations of  $\Gamma_{\text{surface}}$  are relatively high ( $> -7$  dB).

Fig. 9d shows  $\Gamma_{\text{surface}}$  over Belt and Jackboot Bays. Like Madigan Gulf,  $\Gamma_{\text{surface}}$  is high when the salt pan is not flooded. However, unlike Madigan Gulf, once Belt and Jackboot Bays completely flooded,  $\Gamma_{\text{surface}}$  was, at times, very low. Although we cannot definitively prove this, we suspect that this could be due to the fact that Belt Bay is the deepest point in Lake Eyre and could be deep enough for ripples or even surface waves to form once that part of the lake is completely filled. The decrease in  $\Gamma_{\text{surface}}$  in Belt Bay can be seen in Fig. 6, where observations within the middle of Belt Bay have lower  $\Gamma_{\text{surface}}$  when flooded than when dry.

## 7. Discussion

The observations over the Amazon and Lake Eyre shown in Figs. 8 and 9 follow general trends exhibited by the simple model proposed here. As shown in the model, the salt flats of Lake Eyre only produced small increases in  $\Gamma_{\text{surface}}$  for increasing surface water, whereas  $\Gamma_{\text{surface}}$  in the Amazon increased significantly for small increases in surface water.

Perhaps somewhat paradoxically, the rougher the terrain, the easier it would be to retrieve inundation extent using CYGNSS data. This is because an increased amount of water within one footprint will both increase the dielectric constant of the surface in addition to suppressing surface roughness (provided that the water is smoother than the land).

If the land is already as smooth or smoother than the water, then reflectivity only increases due to the increase in the dielectric constant. This then begs the question—which end member scenario is most of Earth's land surface closest to? If most of the Earth's surface is as flat as Lake Eyre, then the confounding effects of soil moisture, not to mention the uncertainties in transmitted power mentioned earlier, could lead to large uncertainties in retrieved inundation extent. If, on the other hand, the Earth's surface tends to be significantly more rough, then retrieving inundation extent could be a more simple process. It is our opinion that the majority of natural surfaces tend to lie within the middle of the two end member scenarios proposed here, though quantifying this will be the subject of future research.

As the observations from Belt and Jackboot Bays show, the decrease in  $\Gamma_{\text{surface}}$  due to the presence of ripples or waves could make retrieving inundation extent for deeper and larger bodies of water more difficult. However, given that the locations and extents of deeper and larger bodies of inland water, like reservoirs, are generally well known, we do not think this significantly detracts from the overall utility of GNSS-R to be used for transient flooding events.

## 8. Conclusions

This paper presented a simple, quasi-conceptual model that related the observations obtained by CYGNSS to inundation extent. Observations, to a first order, fit the general trends exhibited by the model. Future efforts should be made to obtain sufficient micro-scale surface roughness data such that a robust validation study can be performed.

CYGNSS has important implications for hydrologic applications that require data to be collected more frequently and at a high spatial resolution. Although the current constellation of eight satellites requires a few days to provide sufficient coverage over land, if there is enough interest from the hydrologic community it is not unreasonable to assume that more satellites will be launched in the coming years, vastly improving temporal coverage.

## Declaration of Competing Interest

The authors declare that they have no known competing financial interests or personal relationships that could have appeared to influence the work reported in this paper.

## Acknowledgements

We would like to acknowledge funding for this work by NASA award 80NSSC18K1430. We would also like to thank members of the CYGNSS team for their efforts in providing the highest quality GNSS-R data possible.

Appendix A. Appendix

A.1. In situ observations of soil moisture versus model simulations

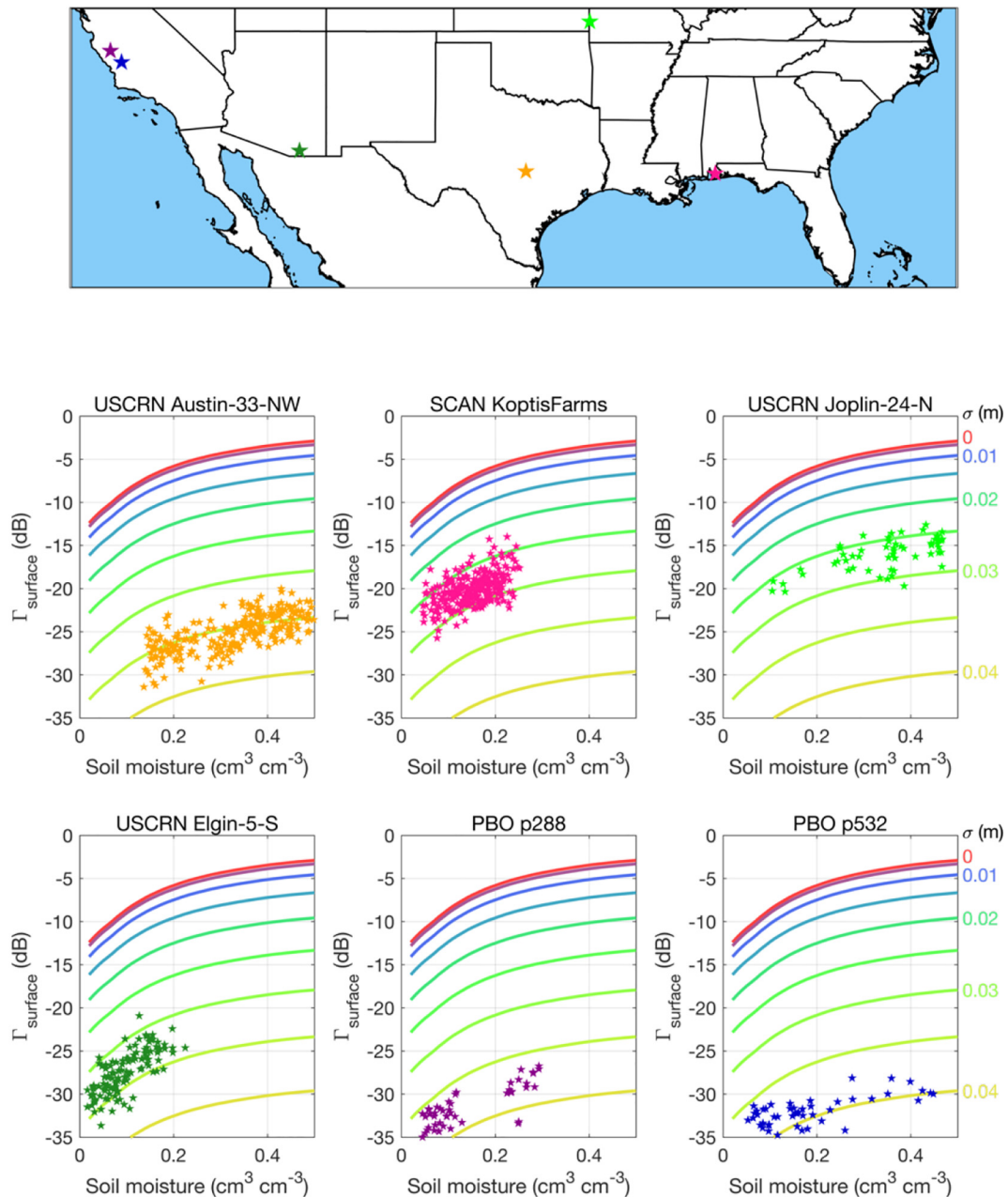


**Fig. A1.** The relationship between in situ soil moisture and CYGNSS observations of  $\Gamma_{surface}$ , for six in situ stations in the United States (colored stars). Locations of each station are indicated by the corresponding colored stars in the map. Also shown are model simulations of how soil moisture and  $\Gamma_{surface}$  should vary, depending on  $\sigma$ . In situ data were obtained from the International Soil Moisture Network database (Dorigo et al., 2011). Observations of  $\Gamma_{surface}$  were considered collocated with each station if the specular reflection point fell within 10 km of the station.

Fig. A1 shows how CYGNSS observations of  $\Gamma_{surface}$  vary with soil moisture, for six in situ soil moisture stations from three different networks (SCAN, USCRN, and PBO). Model simulations agree with the empirical relationships. For example, observations of  $\Gamma_{surface}$  near USCRN Elgin-5-S show the same trend with soil moisture observed in the model, if the surface roughness ( $\sigma$ ) near the station is between 4 and 4.5 cm. Similarly,  $\Gamma_{surface}$  near USCRN Joplin-24-N agrees with model simulations for cases when  $\sigma$  is between 3 and 4 cm.

Although the in situ observations shown in Fig. A1 show the trends observed in the model, we are not able to conclusively validate them without accurate ancillary measurements of  $\sigma$ . If the model is correct, then the  $\sigma$  near the two PBO stations in Fig. A1 is higher than the other stations, with Koptis Farms and Joplin-24-N indicating the smallest  $\sigma$ . When we compared what Fig. A1 indicated in terms of  $\sigma$  with the SMAP static map of  $\sigma$  at the 9 km scale, however, we found large discrepancies. In particular, the SMAP estimates of  $\sigma$  for all stations shown in Fig. A1 were less than 1.15 cm, which is much less than, for example, the 5 cm of roughness indicated by the model for the PBO stations. However, when viewed globally, 99.9% of the SMAP roughness values at the 9 km scale are less than 1.75 cm (Peng et al., 2019). Some researchers are showing that, at least for agricultural landcover types, the SMAP estimates of  $\sigma$  are likely underestimating true  $\sigma$ , given discrepancies between estimated and measured  $\sigma$  and resulting dry biases in the SMAP soil moisture retrievals themselves (Hornbuckle et al., 2017).

A.2. Example of water mask for Lake Eyre

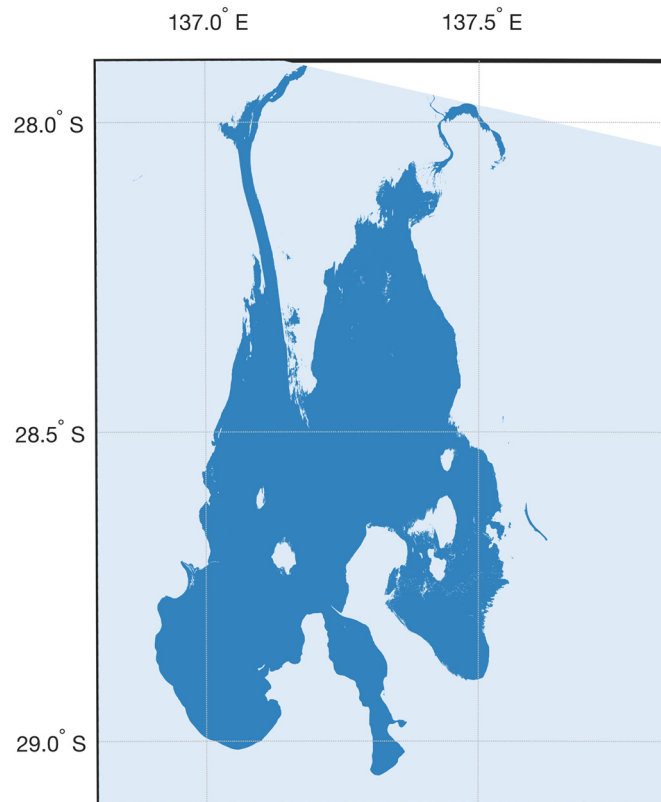


Fig. A2. Water mask derived from Lake Eyre for the MNDWI data shown in Fig. 6d with a threshold value of 0.7. Dark blues indicate regions that are open water, and light blues are regions that are not inundated. The area in white has no data, as it was the edge of the Landsat tile.

A.3. Variations in model simulations based on incidence angle

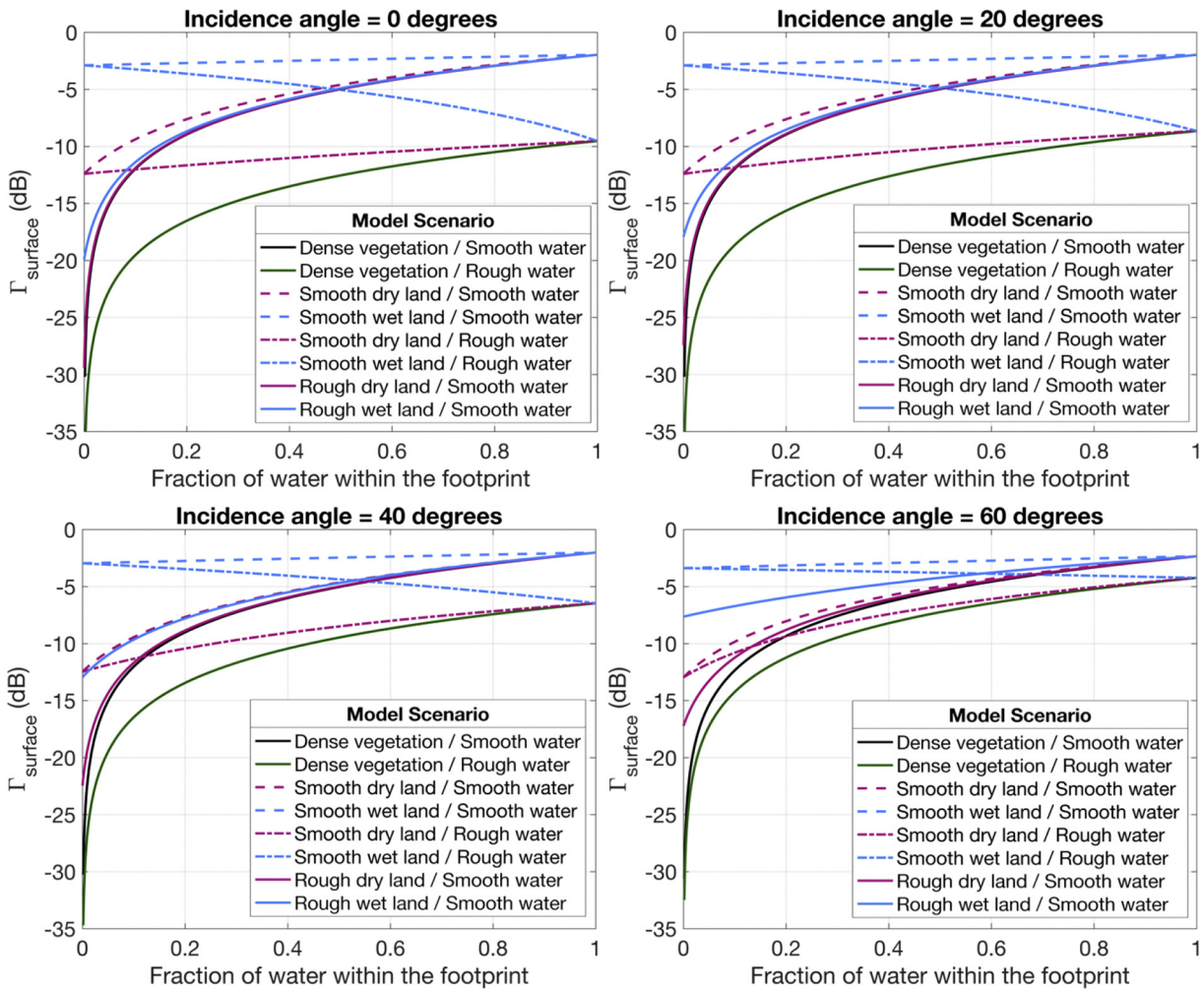
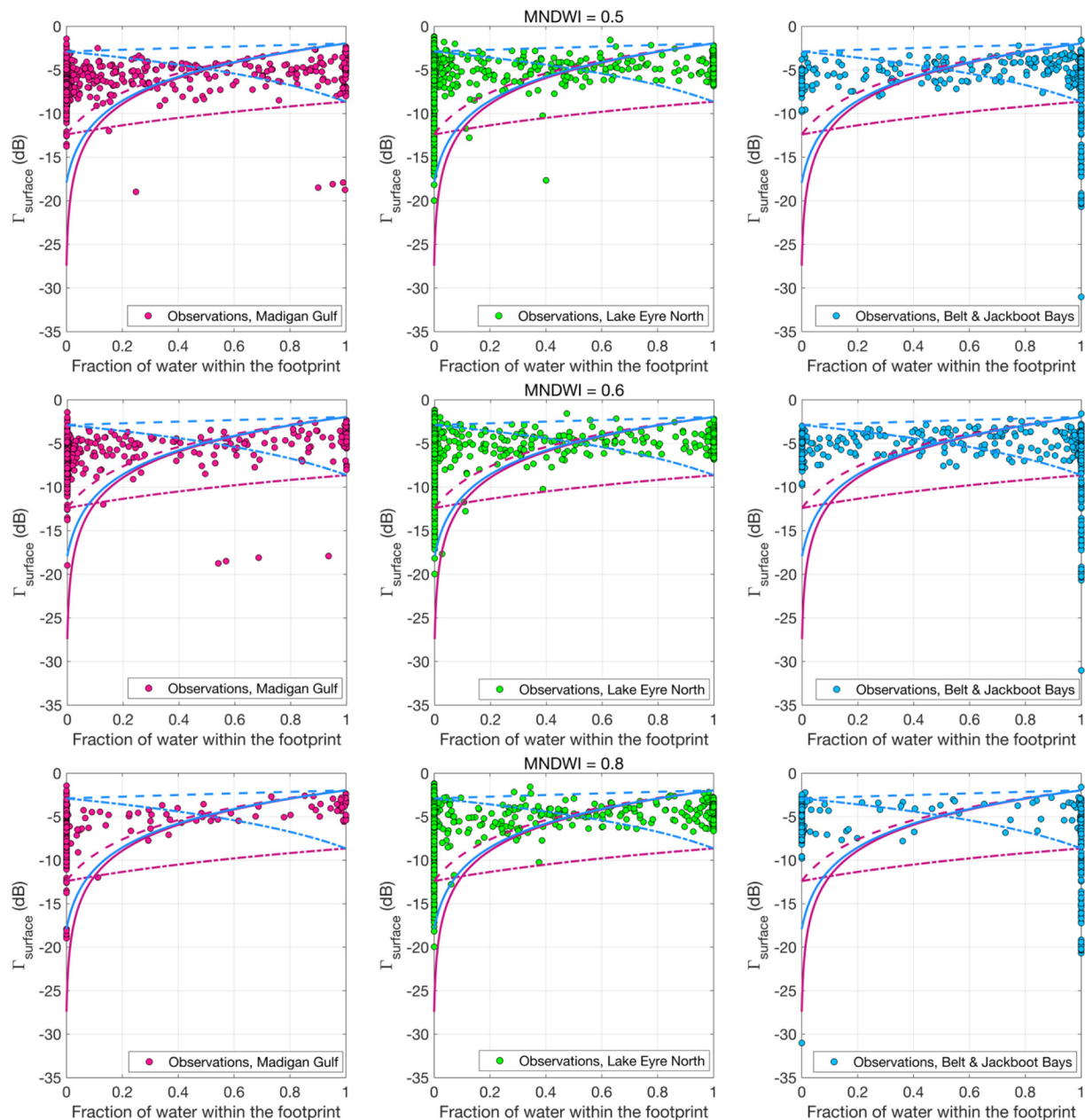


Fig. A3. Model simulations showing how varying the incidence angle will alter the relationship between the fraction of water within a CYGNSS footprint and  $\Gamma_{surface}$ . Fig. A3 shows how the model results presented in the main text would change, depending on incidence angle. As incidence angle increases, the effect of  $\sigma$  on  $\Gamma_{surface}$  decreases. Lower incidence angles result in lower  $\Gamma_{surface}$  for the same value of  $\sigma$ , as higher incidence angles.

## A.4. Changing the MNDWI threshold over Lake Eyre



**Fig. A4.** For Lake Eyre, how altering the MNDWI threshold will affect the fraction of water within the CYGNSS footprint, for thresholds of 0.5, 0.6, and 0.8. Changing the threshold used to convert MNDWI to a binary water mask over Lake Eyre does not significantly change the results presented in this paper. A threshold of 0.7 was used in the main text, and Fig. A4 shows results from three different thresholds (0.5, 0.6, and 0.8). These results are very similar to those presented in the main text. Lowering the threshold below 0.5 was not realistic, as doing so falsely identified the dry salt pans as water.

## References

- Bahafza, B.R., 2005. *Radar Systems Analysis and Design Using MATLAB*, 2nd, Editio. ed. Chapman and Hall/CRC, Boca Raton.
- Balakhder, A.M., Al-Khalidi, M.M., Johnson, J.T., 2019. On the coherency of ocean and land surface specular scattering for GNSS-R and signals of opportunity systems. *IEEE Trans. Geosci. Remote Sens.* 57, 10426–10436.
- Baqir, M., Sobani, Z.A., Bhamani, A., Bham, N.S., Abid, S., Farook, J., Beg, M.A., 2012. Infectious diseases in the aftermath of monsoon flooding in Pakistan. *Asian Pac. J. Trop. Biomed.* 2, 76–79.
- Burgin, M., Clewley, D., Lucas, R.M., Moghaddam, M., 2011. A generalized radar back-scattering model based on wave theory for multilayer multispecies vegetation. *IEEE Trans. Geosci. Remote Sens.* 49, 4832–4845. <https://doi.org/10.1109/TGRS.2011.2172949>.
- Camps, A., Park, H., Pablos, M., Foti, G., Gommenginger, C.P., 2016. Sensitivity of GNSS-R Spaceborne observations to soil moisture and vegetation. *IEEE J. Sel. Top. Appl. Earth Obs. Remote Sens.* 9, 4730–4742.
- Chew, C., Small, E., 2018. Soil moisture sensing using Spaceborne GNSS reflections: comparison of CYGNSS reflectivity to SMAP soil moisture. *Geophys. Res. Lett.* 45, 4049–4057. <https://doi.org/10.1029/2018GL077905>.
- Chew, C., Shah, R., Zuffada, C., Hajj, G., Masters, D., Mannucci, A.J., 2016. Demonstrating soil moisture remote sensing with observations from the UK TechDemoSat-1 satellite mission. *Geophys. Res. Lett.* 43. <https://doi.org/10.1002/2016GL068189>.
- Chew, C., Reager, J.T., Small, E., 2018a. CYGNSS data map flood inundation during the 2017 Atlantic hurricane season. *Sci. Rep.* 8. <https://doi.org/10.1038/s41598-018-27673-x>.
- Chew, C., Small, E., Podest, E., 2018b. Monitoring land surface hydrology using CYGNSS. In: *IGARSS 2018. IEEE 2018 International Geoscience and Remote Sensing*

- Symposium.
- Clapp, R.B., 1946. A Theoretical and Experimental Study of Radar Ground Return. Radiation Laboratory, Massachusetts Institute of Technology, Cambridge, Mass.
- Clarizia, M.P., Gommenginger, C.P., Gleason, S., Srokosz, M.A., Galdi, C., Di Bisceglie, M., 2009. Analysis of GNSS-R delay-Doppler maps from the UK-DMC satellite over the ocean. *Geophys. Res. Lett.* 36.
- De Roo, R.D., Ulaby, F.T., 1994. Bistatic specular scattering from rough dielectric surfaces. *IEEE Trans. Antennas Propag.* 42, 220–231. <https://doi.org/10.1109/8.277216>.
- De Roo, R.D., Ulaby, F.T., 1996. A Modified Physical Optics Model of the Rough Surface Reflection Coefficient, in: *IEEE Antennas and Propagation Society International Symposium*. Baltimore, MD.
- Defourny, P., Schouten, L., Bartalev, S., Bontemps, S., Caccetta, P., de Wit, A.J.W., Di Bella, C., Gerard, B., Giri, C., Gond, V., Hazeu, G.W., Heinemann, A., Herold, M., Knoop, J., Jaffrain, G., Latifovic, R., Lin, H., Mayaux, P., Mucher, C.A., Nonguierma, A., Stibig, H.J., Van Bogaert, E., Vancutsem, C., Bicheron, P., Leroy, M., Arino, O., 2009. Accuracy Assessment of a 300 M Global Land Cover Map: The GlobCover Experience, in: *33rd International Symposium on Remote Sensing of Environment (ISRSE)*. Stresa, Italy, pp. 1–5.
- Dobson, M.C., Ulaby, F.T., Hallikainen, M.T., El-Rayes, M.A., 1985. Microwave dielectric behavior of wet soil-part II: dielectric mixing models. *IEEE Trans. Geosci. Remote Sens.* GE-23, 35–46. <https://doi.org/10.1109/TGRS.1985.289498>.
- Dorigo, W.A., Wagner, W., Hohensinn, R., Hahn, S., Paulik, C., Xaver, A., Gruber, A., Drusch, M., Mechenburg, S., van Oevelen, P., Robock, A., Jackson, T., 2011. The international soil moisture network: a data hosting facility for global in situ soil moisture measurements. *Hydrol. Earth Syst. Sci.* 15, 1675–1698.
- Du, J., Kimball, J.S., Galantowicz, J., Kim, S.-B., Chan, S., Reichle, R., Jones, L., Watts, J., 2018. Assessing global surface water inundation dynamics using combined satellite information from SMAP, AMSR2 and Landsat. *Remote Sens. Environ.* 213, 1–17.
- Durack, P.J., Wijffels, S.E., Matear, R.J., 2012. Ocean salinities reveal strong global water cycle intensification during 1950 to 2000. *Science* (80-. ) 336, 455–458.
- Egido, A., 2013. GNSS Reflectometry for Land Remote Sensing Applications, PhD Thesis.
- Ferrazzoli, P., Guerriero, L., Pierdicca, N., Rahmoune, R., 2011. Forest biomass monitoring with GNSS-R: theoretical simulations. *Adv. Sp. Res.* 47, 1823–1832. <https://doi.org/10.1016/j.asr.2010.04.025>.
- Foti, G., Gommenginger, C., Jales, P., Unwin, M., Shaw, A., Robertson, C., Roselló, J., 2015. Spaceborne GNSS reflectometry for ocean winds: first results from the UK TechDemoSat-1 mission. *Geophys. Res. Lett.* 42, 5435–5441. <https://doi.org/10.1002/2015GL064204>.
- Fuks, I.M., 2001. Wave diffraction by a rough boundary of an arbitrary plane-layered medium. *IEEE Trans. Antennas Propag.* 49, 630–639. <https://doi.org/10.1109/8.923325>.
- Geudtner, D., Torres, R., 2012. Sentinel-1 system overview and performance. 2012 IEEE International Geoscience and Remote Sensing Symposium, Munich. pp. 1719–1721. <https://doi.org/10.1109/IGARSS.2012.6351191>.
- Gillespie, T.W., Chu, J., Frankenberg, E., Thomas, D., 2007. Assessment and prediction of natural hazards from satellite imagery. *Prog. Phys. Geogr. Earth Environ.* 31, 459–470.
- Gleason, S., Ruf, C., O'Brien, A., McKague, D., 2019. The CYGNSS level 1 calibration algorithm and error analysis based on on-orbit measurements. *IEEE J. Sel. Top. Appl. Earth Obs. Remote Sens.* 12, 37–49.
- Gopal, B., 2013. Future of wetlands in tropical and subtropical Asia, especially in the face of climate change. *Aquat. Sci.* 75, 39–61.
- Hallikainen, M.T., Ulaby, F.T., Dobson, M.C., El-Rayes, M.A., Wu, L.-K., 1985. Microwave dielectric behavior of wet soil-part I: empirical models and experimental observations. *Geosci. Remote Sensing*, *IEEE Trans.* GE-23, 25–34. <https://doi.org/10.1109/TGRS.1985.289497>.
- Hornbuckle, B., Walker, V., Eichinger, B., Wallace, V., Yildirim, E., 2017. Soil Surface Roughness Observed during SMAPVEX16-IA and its Potential Consequences for SMOS and SMAP, in: *International Geoscience and Remote Sensing Symposium (IGARSS)*2. Ft. Worth, Texas.
- Huntington, T.G., 2006. Evidence for intensification of the global water cycle: review and synthesis. *J. Hydrol.* 319, 83–95.
- Jensen, K., McDonald, K., Podest, E., Rodríguez-Álvarez, N., Horna, V., Steiner, N., 2018. Assessing L-band GNSS-Reflectometry and imaging radar for detecting sub-canopy inundation dynamics in a tropical wetlands complex. *Remote Sens.* 10, 1431.
- Kaatze, U., 1989. Complex permittivity of water as a function of frequency and temperature. *J. Chem. Eng. Data* 34, 371–374.
- Katzberg, S.J., Garrison, J.L., 1996. Utilizing GPS to determine Ionospheric delay over the ocean. *Nasa Tech. Memo TM-4750* 1–16. (Doi:10.1.1.31.3748).
- Lang, R.H., Sighu, J.S., 1983. Electromagnetic backscattering from a layer of vegetation: a discrete approach. *IEEE Trans. Geosci. Remote Sens.* GE-21, 62–71.
- Masters, D.S., 2004. Surface remote sensing applications of GNSS bistatic radar: soil moisture and aircraft altimetry. *ProQuest Diss. Theses* 3153856, 224.
- Mladenova, I., Jackson, T.J., Bindlish, R., Hensley, S., 2013. Incidence angle normalization of radar backscatter data. *IEEE Trans. Geosci. Remote Sens.* 51, 1791–1804.
- Morris, M., Chew, C., Reager, J.T., Shah, R., Zuffada, C., 2019. A novel approach to monitoring wetland dynamics using CYGNSS: Everglades case study. *Remote Sens. Environ.* 233. <https://doi.org/10.1016/j.rse.2019.111417>.
- Nghiem, S.V., Zuffada, C., Shah, R., Chew, C., Lowe, S.T., Mannucci, A.J., Cardellach, E., Brakenridge, G.R., Geller, G., Rosenqvist, A., 2017. Wetland monitoring with global navigation satellite system reflectometry. *Earth Sp. Sci.* 4. <https://doi.org/10.1002/2016EA000194>.
- O'Brien, A., Johnson, J.T., 2017. Comparing the CYGNSS Simulator Forward Scattering Model with TDS-1 and CYGNSS on-Orbit DDMs, in: *2017 IEEE International Geoscience and Remote Sensing Symposium*. Fort Worth, TX.
- Pekel, J.-F., Cottam, A., Gorelick, N., Belward, A.S., 2016. High-resolution mapping of global surface water and its long-term changes. *Nature* 540, 418–422.
- Peng, J., Mohammed, P., Chaubell, J., Chan, S., Kim, S., Das, N., Dunbar, S., Bindlish, R., Xu, X., 2019. Soil Moisture Active Passive (SMAP) L1-L3 Ancillary Static Data, Version 1. Boulder, Colorado USA. NASA National Snow and Ice Data Center Distributed Active Archive Center. <https://doi.org/10.5067/HB8BPJ13TDQJ>, Accessed date: 2 January 2020.
- Pierdicca, N., Guerriero, L., Giusto, R., Brogioni, M., Egido, A., 2014. SAVERS: a simulator of GNSS reflections from bare and vegetated soils. *IEEE Trans. Geosci. Remote Sens.* 52, 6542–6554. <https://doi.org/10.1109/TGRS.2013.2297572>.
- Rodríguez-Álvarez, N., Podest, E., Jensen, K., McDonald, K., 2019. Classifying inundation in a tropical wetlands complex with GNSS-R. *Remote Sens.* 11, 1053.
- Ruf, C., Gleason, S., Jelenak, Z., Katzberg, S., Ridley, A., Rose, R., Scherrer, J., Zavorotny, V., 2012. The CYGNSS nanosatellite constellation hurricane mission, in: *2012 IEEE International Geoscience and Remote Sensing Symposium*. pp. 214–216.
- Ruf, C., Chew, C.C., Lang, T., Morris, M., Nave, K., Ridley, A., Balasubramanian, R., 2018. A new paradigm in earth environmental monitoring with the CYGNSS small satellite constellation. *Sci. Rep.* 8.
- Schroeder, R., McDonald, K.C., Chapman, B.D., Jensen, K., Podest, E., Tessler, Z.D., Bohn, T.J., Zimmermann, R., 2015. Development and evaluation of a multi-year fractional surface water data set derived from active/passive microwave remote sensing data. *Remote Sens.* 7, 16688–16732.
- Schumann, G., Hostache, R., Puech, C., Hoffman, L., Matgen, P., Pappenberger, F., Pfister, L., 2007. High-resolution 3-D flood information from radar imagery for flood hazard management. *IEEE Trans. Geosci. Remote Sens.* 45, 1715–1725.
- Snapir, B., Hobbs, S., Waine, T.W., 2014. Roughness measurements over an agricultural soil surface with structure from motion. *ISPRS J. Photogramm. Remote Sens.* 96, 210–223.
- Steigenberger, P., Tholert, S., Montenbruck, O., 2019. Flex power on GPS block IIR-M and IIF. *GPS Solut.* 23. <https://doi.org/10.1007/s10291-018-0797-8>.
- Thomsen, L.M., Baartman, J.E.M., Barneveld, R.J., Starkloff, T., Stolte, J., 2015. Soil surface roughness: comparing old and new measuring methods and application in a soil erosion model. *SOIL* 1, 399–410.
- Ulaby, F.T., Bativala, P.P., Dobson, M.C., 1978. Microwave backscatter dependence on surface roughness, soil moisture, and soil texture: part I-bare soil. *IEEE Trans. Geosci. Remote Sens.* 16, 286–295.
- Ulaby, F.T., Sarabandi, K., McDonald, K., Whitt, M., Dobson, M.C., 1990. Michigan microwave canopy scattering model. *Int. J. Remote Sens.* 11, 1223–1253.
- Xu, H., 2006. Modification of normalised difference water index (NDWI) to enhance open water features in remotely sensed imagery. *Int. J. Remote Sensing* 2 (27), 3025–3033.